1

HIGH-ORDER ENTROPY-BASED CLOSURES FOR LINEAR TRANSPORT IN SLAB GEOMETRY

CORY D. HAUCK †

Abstract. We compute high-order entropy-based (M_N) models for a linear transport equation on a one-dimensional, slab geometry. We simulate two test problems from the literature: the two-beam instability and the plane-source problem. In the former case, we compute solutions for systems up to order $N = 5$; in the latter, up to $N = 15$. The most notable outcome of these results is the existence of shocks in the steady-state profiles of the two-beam instability for all odd values of N.

1. Introduction In transport and kinetic theory, moment models are used as a means to reduce the size of the state space required for a kinetic description while still maintaining basic features of a kinetic model. They do so by replacing the velocity component of phase space by a finite number of velocity moments. Moment models are commonly derived using an approximate reconstruction of the kinetic description from these moments. The reconstruction prescribes a closure, i.e., a recipe for expressing the moment model as a closed system of the retained moments. *Entropy-based methods* specify this reconstruction as the solution to a constrained, convex optimization problem. In many situations, the cost functional for the optimization problem is directly related to the kinetic entropy of the system. In other cases, it simply enforces physically relevant features. The benefit of the entropy approach is a reduced model which retains fundamental properties from the kinetic formalism not found in traditional moment models such as hyperbolicity, entropy dissipation, and positivity. The main disadvantage of the entropy approach is that, unlike traditional moment models, the entropy-based kinetic reconstruction can rarely be expressed as an analytic function of the given moments. Thus the optimization problem must be solved numerically, via the associated dual problem. This can increase computational costs significantly.

Recent advances in both analysis and implementation of entropy-based methods have been made in several application areas. For gas dynamics, the formal properties of entropy-based models were elucidated in [27]. However, it is also known [18, 21, 22, 39] that the defining optimization problem in this case is ill-posed. As a result, alternative approaches are currently being pursued which regularize the problem in some suitable fashion. (See [16] and references therein.) For charge transport in semiconductors, the issue of ill-posedness also exists for the so-called parabolic band approximation [30, p.69]. However, for experimental dispersion relations or for more realistic approximations, like the Kane dispersion relation [2, p.3], the optimization problem is well-posed [23]. Indeed recent simulations [38] have shown reasonable agreement with Monte-Carlo results.

In the field of radiative transport, moments are typically taken with respect to functions of the angular component of the microscopic particle velocity only. A general theoretic framework was laid out in [10], although most of the computational results

*February 1, 2010

†Computational Mathematics Group, Computer Science and Mathematics Division, Oak Ridge National Laboratory, Oak Ridge, TN 37831 USA, (hauckc@ornl.gov).

have been limited to the so-called Minerbo, or M_1, model or variations thereof [5, 11, 13, 32] which track moments of the kinetic distribution with respect to polynomials up to degree one. The reason for this limitation is that, beyond the M_1 model, the defining optimization problem is especially hard to solve for highly anisotropic distributions, which commonly occur in transport applications. A recent and notable advance in this direction is the recent work in [33, 42], where the authors simulate the M_2 model (the next model in the hierarchy, which tracks moment with respect to polynomials up to degree two) for one-dimensional, slab geometries. This simulation is done using a clever procedure to bypass the optimization problem completely. The most powerful aspect of this approach is the ability to handle beam-like distributions with relative ease. The procedure is based on a look-up table and hence, becomes less practical when more moments are added (either by increasing the polynomial degree further or by adding more dimensions). Interpolation can also be used to reduce the number of entries in the look-up table, but exactly how such an interpolation effects hyperbolicity of the moment system is unclear. Thus, one must consider attacking the optimization problem head-on. In the future, it is likely that a combination of the two methods will be most effective.

In spite of the heavy computational overhead of solving difficult optimization problems, the entropy-based approach still has practical merit for large-scale, massively parallel computations that one might see in a complex multi-physics application. This is due to the emerging paradigm in parallel computing in which data transfer—not floating point operations—is the bottleneck to efficient computation [31, 43]. In particular, though the optimization uses many function evaluations to find a solution, the solver for updating the moment equations requires the same amount of data transfer between computational cells as it would for a conventional, algebraic closure.

In this paper, we consider entropy-based models, including and beyond M_1 and M_2, for the simple case of linear transport in slab geometries, utilizing the Maxwell-Boltzmann entropy as the cost functional in our optimization problem. The moment equations in this setting are formulated in Section 2. In Section 3, we present the kinetic scheme used to implement them. In Section 4, we present numerical results for two test cases found elsewhere in the literature. Neither of these test cases severely tests the limits of our optimization algorithm (a blackbox MATLAB solver). Rather, the goal is to gain some insight about what can be gained by going to higher-order closures. Section 5 is devoted to conclusions and discussion.

2. Entropy-Based Moment Equations We assume a distribution of particles of a single unit speed which are absorbed by or isotropically scattered off of a background material medium with slab geometry. We let $x \in (x_1, x_2)$ be the scalar coordinate along the axis perpendicular to the slab; $\mu \in [-1, 1]$ is the cosine of the angle between the x-axis and the direction of particle travel; $t \geq 0$ is time; and for any measurable function $g = g(\mu)$,

$$\langle g \rangle \equiv \int_{-1}^{1} g(\mu) d\mu \,. \tag{2.1}$$

The state of the particles is characterized by a non-negative function $F(x, \mu, t)$.

The material is characterized by non-negative variables $\sigma_{\mathrm{s}}(x)$, $\sigma_{\mathrm{a}}(x)$, and $\sigma_{\mathrm{t}}(x) = \sigma_{\mathrm{s}}(x) + \sigma_{\mathrm{s}}(x)$ which are the scattering, absorption, and total cross-sections, respectively, of the material. Each cross-section is the reciprocal of the mean-free-path between particle interactions of a given type. The function S is an external source,

which in general may depend on properties of the material. However, for the test cases in Section 4, we will take $S = 0$.

In this setting, the relevant transport equation for F takes the form [6, 28, 37]

$$\partial_t F + \mu \partial_x F + \sigma_{\mathrm{t}} F = \frac{\sigma_{\mathrm{s}}}{2} \langle F \rangle + S \tag{2.2}$$

and is supplemented by boundary conditions and initial conditions

$$F(x_1, \mu, t) = F_1(\mu, t)\,, \quad \mu > 0\,, \tag{2.3a}$$
$$F(x_2, \mu, t) = F_2(\mu, t)\,, \quad \mu < 0\,, \tag{2.3b}$$
$$F(x, \mu, 0) = F_0(x, \mu)\,. \tag{2.3c}$$

Here F_0, F_1, and F_2 are given.

Moment equations for (2.2) are typically based on angular averages with respect to Legendre polynomials. To derive an order N system, we collect the first $N+1$ Legendre polynomials into a vector-valued function $\mathbf{m} : [-1, 1] \to \mathbb{R}^{N+1}$. Exact equations for the moments $\mathbf{u}(x, t) = [u_0, \ldots, u_N]^T := \langle \mathbf{m} F(x, \cdot, t) \rangle$ are found by multiplying the transport equation (2.2) by $\mathbf{m}$ and integrating over all angles. This gives the system

$$\partial_t \mathbf{u} + \partial_x \langle \mu \mathbf{m} F \rangle + \sigma_{\mathrm{t}} \mathbf{u} = \frac{\sigma_{\mathrm{s}}}{2} Q \mathbf{u} + \mathbf{s}\,, \tag{2.4}$$

where

$$Q_{lk} := \delta_{lk} \delta_{l,0} \quad \text{and} \quad \mathbf{s} := \langle \mathbf{m} S \rangle\,. \tag{2.5}$$

Boundary conditions for the moment system are not so easily expressed since kinetic data is only given for values of μ which correspond to incoming data. Indeed, the issue of proper boundary conditions remains an open question, although some progress has been made for linear systems [24–26, 36].[1]

The moment system (2.4) is closed by substituting the approximation

$$F(x, \mu, t) \simeq \mathcal{F}(\mathbf{u}(x, t), \mathbf{m}(\mu)) \tag{2.6}$$

into (2.4), where the reconstruction $\mathcal{F}$ satisfies the consistency relation

$$\langle \mathbf{m} \mathcal{F}(\mathbf{u}, \mathbf{m}) \rangle = \mathbf{u}\,. \tag{2.7}$$

The resulting system takes the form

$$\partial_t \mathbf{u} + \partial_x \langle \mu \mathbf{m} \mathcal{F}(\mathbf{u}, \mathbf{m}) \rangle + \sigma_{\mathrm{t}} \mathbf{u} = \frac{\sigma}{2} Q \mathbf{u} + \mathbf{s}\,. \tag{2.8}$$

The question of whether (2.8) can accurately capture the dynamics of the original transport equation depends heavily on the details of $\mathcal{F}$.

Entropy-based methods generate a closure by prescribing $\mathcal{F}$ as the solution of a constrained, convex optimization problem. To be more specific, given a strictly convex mapping $\eta \colon \mathbb{R} \ni z \mapsto \eta(z) \in \mathbb{R}$, $\mathcal{F}$ solves

$$\begin{aligned} &\text{minimize} && \langle \eta(f) \rangle \\ &\text{subject to} && \langle \mathbf{m} f \rangle = \mathbf{u}\,. \end{aligned} \tag{2.9}$$

[1] For computations presented later in the paper, we prescribe boundary conditions that are reasonable, but not entirely consistent with the kinetic boundary conditions.

If a solution exists, it takes the form [27]

$$\mathcal{F}(\mathbf{u},\mathbf{m}) = G_{\hat{\boldsymbol{\alpha}}(\mathbf{u})} := \eta_y^*\left(\hat{\boldsymbol{\alpha}}(\mathbf{u})^T\mathbf{m}\right)\,, \tag{2.10}$$

where $\eta^*\colon \mathbb{R} \ni y \mapsto \eta^*(y) \in \mathbb{R}$ is the Legendre dual of η and the vector $\hat{\boldsymbol{\alpha}} : \mathbf{u} \in \mathbb{R}^{N+1} \mapsto \hat{\boldsymbol{\alpha}}(\mathbf{u}) \in \mathbb{R}^{N+1}$ solves the dual problem

$$\text{minimize}_{\boldsymbol{\alpha}\in\mathbb{R}^{N+1}}\ \left\{\left\langle \eta^*(\boldsymbol{\alpha}^T\mathbf{m})\right\rangle - \boldsymbol{\alpha}^T\mathbf{u}\right\}\,. \tag{2.11}$$

In particular, first-order optimality conditions for (2.11) recover the consistency relation (2.7):

$$\left\langle \mathbf{m}\eta_y^*(\hat{\boldsymbol{\alpha}}^T\mathbf{m})\right\rangle = \mathbf{u}\,. \tag{2.12}$$

Furthermore, it is straight-forward to show (following arguments in [10,27], for example) that the moment system dissipates the strictly convex entropy $h(\mathbf{u}) := \langle \eta(G_{\hat{\boldsymbol{\alpha}}(\mathbf{u})})\rangle$ and that, when written in terms of $\hat{\boldsymbol{\alpha}}$, the entropy-based moment system is symmetric hyperbolic.

Different choices of η lead to different closures. In gas dynamics applications, one typically uses the Maxwell-Boltzmann entropy; for fermions, the Fermi-Dirac entropy; for bosons (as in photon transport), the Bose-Einstein entropy. In some cases, the choice of entropy is not directly related to the physics of the problem. For example, the choice $\eta(z) = z^2/2$ leads to the well-known P_N equations [7, 28, 37]. For the purposes of this paper, we assume classical particles with a slight variation of the Maxwell-Boltzmann entropy

$$\eta(z) = z\log(z) - z \tag{2.13}$$

and Legendre dual $\eta^*(y) = e^y$. In this case, the exponential form ensures that the reconstruction is always a positive function.

3. Implementation with a Kinetic Scheme We implement the moment equations from the previous section using a kinetic scheme [8, 9, 17, 34, 35]. In a conventional approach, one first takes moments of the kinetic equations and then finds a valid spatial discretization of the resulting moment system. With a kinetic scheme, these steps are reversed: one first determines a valid discretization of the kinetic equation and then takes moments of this discretization. The benefit of this approach is that it avoids the direct computation of eigenvalues and (approximate) Riemann solvers for the entropy-based moment systems, which generally cannot by computed by hand.

3.1. Description of the Scheme Let $\{x_j\}_{j=1}^J$ be an evenly spaced set of mesh points which serve as the centers of cells $I_j = (x_{j-1/2}, x_{j+1/2})$ of width Δx. For simplicity of notation, we assume here that all material cross-sections are constant.[2] A semi-discrete, finite-volume formulation of the transport equation is derived by integration in x over each I_j, giving

$$\partial_t F_j + \mu\frac{F_{j+1/2} - F_{j-1/2}}{\Delta x} + \sigma_{\mathrm{t}}F_j = \frac{1}{2}\sigma_{\mathrm{s}}\phi_j + S_j\,. \tag{3.1}$$

Here j subscripts adorn cell averages (in space) and $j\pm1/2$ subscripts denote pointwise values at cell edges, which are approximated by upwinding: for $\mu > 0$, information

[2] Our test problems in the next section will all satisfy this assumption, but there is certainly no limitation that requires it.

comes from the left; for $\mu < 0$, it comes from the right. When applied to (3.1), upwinding gives

$$\partial_t F_j + \max(\mu,0)\frac{F_{j+1/2,\ell} - F_{j-1/2,\ell}}{\Delta x} + \min(\mu,0)\frac{F_{j+1/2,r} - F_{j-1/2,r}}{\Delta x} + \sigma_{\mathrm{t}} F_j = \frac{1}{2}\sigma_{\mathrm{s}}\phi_j + S_j \tag{3.2}$$

where $F_{j+1/2,\ell}$ and $F_{j+1/2,r}$ are values on the right and left sides of the cell edge at $x_{j+1/2}$. A linear approximation of these values is

$$F_{j+1/2,\ell} = F_j + \frac{\Delta x}{2}F_j' \quad \text{and} \quad F_{j+1/2,r} = F_{j+1} - \frac{\Delta x}{2}F_{j+1}' \,, \tag{3.3}$$

where F_j' is an approximation of the spatial gradient in cell j. We use the well-known minmod limiter function:

$$F_j' = \mathrm{minmod}\left\{\frac{F_j - F_{j-1}}{\Delta x}, \frac{F_{j+1} - F_{j-1}}{2\Delta x}, \frac{F_{j+1} - F_j}{\Delta x}\right\} . \tag{3.4}$$

The idea of the limiter is to suppress spurious oscillations in the solution and, in the context of the entropy closure, to ensure that the edge values for F are non-negative.

To obtain an algorithm for $\mathbf{u}_j := \langle \mathbf{m} F_j \rangle$ with the entropy-based closure, we simply integrate the discretization (3.1) of the kinetic equation against the vector $\mathbf{m}$ and replace F_j by $G_j := G_{\hat{\boldsymbol{\alpha}}(\mathbf{u}_j)}$. This gives

$$\partial_t \mathbf{u}_j + \frac{\left\langle \mu \mathbf{m}[G_{j+1/2,\ell} - G_{j-1/2,\ell}]\right\rangle_+}{\Delta x} + \frac{\left\langle \mu \mathbf{m}[G_{j+1/2,r} - G_{j-1/2,r}]\right\rangle_-}{\Delta x} + \sigma_{\mathrm{t}}\mathbf{u}_j = \frac{\sigma_{\mathrm{s}}}{2} Q\mathbf{u}_j + \mathbf{s}_j \tag{3.5}$$

where plus/minus subscripts denote integration over positive/negative ranges of μ (so-called half fluxes), Q is given in (2.5), and $\mathbf{s}_j = \langle \mathbf{m} S_j \rangle$.

Time integration of (3.5) depends on the type of problem. For marching to steady state, first-order explicit Euler is satisfactory. However, for transient solutions, we use the second-order, strong stability preserving, Runge-Kutta (SSP-RK2) method [15, 40]. As a reminder to the reader, if we write the semi-discrete system (3.5) in the abstract form

$$\partial_t \vec{\mathbf{u}} = L(\vec{\mathbf{u}}) \,, \tag{3.6}$$

then the SSP-RK2 method takes the form

$$\vec{\mathbf{u}}^{(1)} = \vec{\mathbf{u}}^n + \Delta t L(\vec{\mathbf{u}}^n) \,, \tag{3.7a}$$

$$\vec{\mathbf{u}}^{n+1} = \frac{1}{2}\vec{\mathbf{u}}^n + \frac{1}{2}\vec{\mathbf{u}}^{(1)} + \frac{1}{2}\Delta t L(\vec{\mathbf{u}}^{(1)}) \,. \tag{3.7b}$$

3.2. Details and Subtleties

In this subsection, we briefly discuss important details of the algorithm and some subtle difficulties. Most of these difficulties arise when solving the dual problem (2.11).

1. **Numerical Integration**. The algorithm requires a quadrature rule to evaluate the half fluxes. We use a Gauss-Legendre quadrature with 20 quadrature points.

Paremeter	Meaning	Value
`MaxFunEvals`	Maximum number of function evaluations allowed	10000
`MaxIter`	Maximum number of iterations allowed	10000
`LargeScale`	Use large-scale algorithm if possible	`off`
`Display`	Level of display	`notify`
`TolFun`	Termination tolerance on the objective function and gradient	$\epsilon \simeq 2.22 \times 10^{-16}$
`TolX`	Termination tolerance on x	$\epsilon \simeq 2.22 \times 10^{-16}$
`GradObj`	Gradient for the objective function defined by the user	`on`
`Hessian`	Hessian for the objective function defined by the user	`off`

TABLE 3.1. *Optimization parameters for* `fminunc`*. Parameter that are not given are set to default values.*

2. **Optimization Parameters**. The entire algorithm is implemented in MATLAB. The bulk of the computation lies in the repeated solution the dual problem (2.11), which we find using the built-in function `fminunc`. Paremeters of interest for `fminunc` are set with the command `optimset` and are given in Table 3.1. All other parameters are set to default values. With the `Hessian` parameter set to `off`, `fminunc` approximates Hessians using finite differences of the gradient.
3. **Difficulties with the optmization**. The built-in function `fminunc` breaks down in regimes near the boundary of so-called *realizability*. A vector $\mathbf{u}$ is said to be *realizable* whenever it is the moment of a non-negative function of μ. The set of realizable vectors forms an open set [22] and, roughly speaking, functions of μ which generate vectors near the boundary of this set are highly anisotropic and beam-like. For example, one can show that certain vectors on the boundary can only be generated by delta functions [33]. When the reconstruction $G_{\hat{\boldsymbol{\alpha}}}$ is highly anisotropic, solving the dual problem for $\hat{\boldsymbol{\alpha}}$ becomes quite difficult, because the Hessian becomes singular. Such cases often occur around discontinuities, singularities, and voids in space. Thus increasing the spatial resolution of the computation typically makes the optimization more difficult. In an effort to avoid the boundary of realizability, the test problems in the following sections are slight modifications of problems found in the literature. In particular, voids are replaced by an isotropic distribution F_{floor}, which is set to a small value. Even with this modification, `fminunc` often terminates prematurely—not because some tolerance criteria is satisfied, but because the approximate Hessian no longer predicts a decrease in the function value. Although the error in approximating the nearly-singular Hessian can be fixed by supplying an exact Hessian, `fminunc` will often still terminate because the ceiling set by `MaxFunEvals` and `MaxIter` is broken. In order to be sure of reasonable accuracy in the solution of the dual problem, we compute the difference between the value $\mathbf{u}_j$ and the moment of the reconstruction $\langle \mathbf{m} G_j \rangle$. For all cases, we have found the maximum difference over the entirety of the calculation to be $O(10^{-8})$.[3] In the meantime, devising a more flexible optimization tool is the focus of ongoing research.
4. **Behavior in diffusive regimes**. The kinetic scheme is very inefficient in

[3] Although we have not done so, one could presumably increase the tolerance parameter `TolFun` to a value of this size to ensure proper termination of `fminunc`.

diffusive regimes, where σ_t is large. Indeed, the formal accuracy of the scheme in space is $O(\sigma_t \Delta x^3)$. (See, for example, the second-order upwind analysis in [20, 29]). Furthermore, because the scheme is explicit, $O(\Delta x/\sigma_t, 1/\sigma_t^2)$ time steps are required for stability. Thus in diffusive regimes, accuracy requirements dictate that the spatial and temporal mesh be small, even if the solution profile varies on an $O(1)$ scale. Fortunately for us, the test cases which we will consider in the next section are not in the diffusive regime; instead σ_t is an $O(1)$ quantity. Even so, practical applications will eventually require more robust algorithms be developed for diffusive or multi-scale problems. Such algorithms are the focus of future efforts.

5. **Implementation of boundary conditions**. As mentioned in Section 2, proper boundary conditions for moment equations are not known. For the kinetic scheme, we set (refer to (2.3))

$$G_{1/2,\ell}(\mu_k, t) = F_1(\mu_k, t) \quad \text{and} \quad G_{J+1/2,r}(\mu_k, t) = F_2(\mu_k, t^n) \tag{3.8}$$

for any μ_k in the quadrature set used to evaluate the integrals in (3.5). While reasonable, this is clearly not the only option. Moreover, it the context of gas dynamics, it has been shown [41] that this condition gives inaccurate results unless the mesh resolves the mean free path. Fortunately, this condition holds for the test problems we consider in the next section. One can also argue that, to be consistent with the moment approach, the kinetic data at the boundaries should be replaced by an reconstruction of the form $G_{\hat{\boldsymbol{\alpha}}}$—that is

$$G_{1/2,\ell}(\mu_k, t) = G_{\boldsymbol{\alpha}_{1/2,\ell}} \quad \text{and} \quad G_{J+1/2,r}(\mu_k, t) = G_{\boldsymbol{\alpha}_{J+1/2,r}} \tag{3.9}$$

where the coefficients $\boldsymbol{\alpha}_{1/2,\ell}$ and $\boldsymbol{\alpha}_{J+1/2,r}$ are determined by $N+1$ moment constraints of the form

$$\left\langle \phi_l G_{\boldsymbol{\alpha}_{J+1/2,r}} \right\rangle = \left\langle \phi_l G_{J+1/2,\ell} \right\rangle_+ + \left\langle \phi_l F_2 \right\rangle_- , \quad \phi_l = \phi_l(\mu) , \quad l = 0, \ldots, N \tag{3.10}$$

on the right boundary, with similar conditions on the left. One could let $\phi_l = m_l$, as is done in [41], but this is not the only possibility.

4. Numerical Results In this section, we present results for two types of problems found in the literature: the two-beam instability and the plane source. For the former, we are interested primarily in steady-state solutions for a purely absorbing material, while for the latter we focus on transient solutions for a purely scattering material. All results are given in terms of the particle concentration $\rho := u_0 \equiv \langle F \rangle$.

4.1. Two-Beam Instability The two-beam instability is a test of a closure's ability to handle multi-modal distributions. In this one-dimensional setting, the material slab is initially in an (almost) vacuum state. Particles enter the domain from the right and left boundary and a steady-state is reached. Under some conditions, the M_1 closure is unable to handle particles moving in opposing directions, and as a result, produces a shock in the steady-state profile [5, 11].

It has been shown recently [33, 42] that, in some cases, the M_2 model and also versions of the M_1 model that use partial moments [13] can produce reasonably accurate results without this unphysical shock. In general, the possibility of shocks in the steady-state profile can be characterized by the following result.

THEOREM 4.1 (Frank [12]). *Assume σ_t and $\mathbf{s}$ are bounded. Let $\mathbf{u}$ be any bounded, weak solution of the steady-state M_N system and let $u_{N+1}(\mathbf{u})$ be the moment of the entropy reconstruction $G_{\hat{\boldsymbol{\alpha}}(\mathbf{u})}$ with respect to the $(N+1)$-th Legendre polynomial m_{N+1}, i.e,*

$$u_{N+1}(\mathbf{u}) := \left\langle m_{N+1} G_{\hat{\boldsymbol{\alpha}}(\mathbf{u})} \right\rangle . \tag{4.1}$$

Then the moments $\{u_1, ..., u_{N+1}\}$ are all continuous on the interior of the spatial domain. Furthermore, a necessary condition for interior discontinuities in the steady-state profile of u_0 is that the mapping

$$\left(\frac{u_1}{u_0}, \ldots, \frac{u_N}{u_0} \right) \mapsto \left(\frac{u_{N+1}}{u_1}, \ldots, \frac{u_{N+1}}{u_N} \right) \tag{4.2}$$

is not injective.

It should be noted, first, that this result generalizes the criteria for the M_1 case that was given in [5] and, second, that other criteria are possible. The proof of this generalization is similar to the argument in [5], but for completeness, we include it in an appendix. Unfortunately, the condition (4.2) is not easily checked for $N > 1$ because, in that case, u_{N+1} can only be computed numerically.

We implement the two-beam instability on a one-dimensional slab covering the interval $[-1, 1]$ in space. The parameter values are

$$\sigma_t = \sigma_a = 2.0 , \qquad S = 0 . \tag{4.3}$$

Thus there is no scattering ($\sigma_s = 0$) and no external source. The initial condition for the kinetic equations is (refer to (2.3))

$$F_0(x, \mu) = F_{\text{floor}} = 0.5 \times 10^{-4} , \tag{4.4}$$

and the boundary conditions are isotropic:

$$F_1(\mu, t) = F_2(\mu, t) = 0.5 . \tag{4.5}$$

Boundary and initial conditions for the kinetic scheme are derived from these. The small, non-zero value for the initial condition is needed to maintain stability with respect to the dual problem (2.11), as discussed in the previous section. We march to steady-state using the kinetic scheme with forward Euler time discretization and time step $\Delta t = 0.3\Delta x$.

Results for the two-beam instability are given in Figures 4.1-4.4. For comparison, we include the exact steady-state concentration, $\rho_{ss} \equiv \langle F_{ss} \rangle$, where

$$F_{ss}(x, \mu) = \begin{cases} 0.5 e^{\frac{-\sigma_a(x+1)}{\mu}} , & \mu > 0 , \\ 0.5 e^{\frac{-\sigma_a(x-1)}{\mu}} , & \mu < 0 , \end{cases} \tag{4.6}$$

and the angular integral is computed with a 20-point Gauss-Legendre quadrature.

In Figure 4.1, we show solutions at time $t = 5.0$, when the solution is essentially at steady-state. Roughly speaking, the solutions improve as N increases, but the even and odd profiles are qualitatively different. The even solutions appear to converge from above near the boundary and from below near the center. They also appear

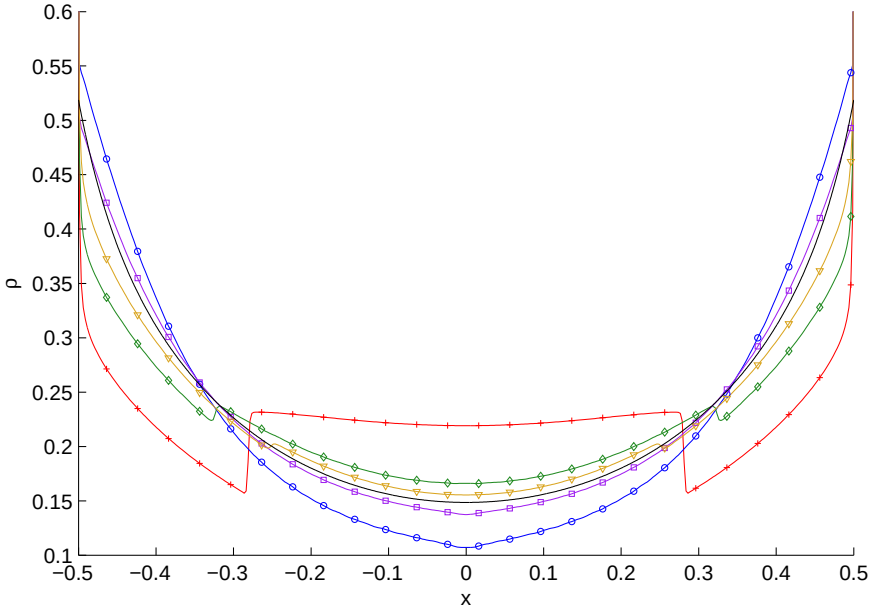

FIG. 4.1. *Steady-state solutions for the two-beam instability. Red pluses are M_1; blue circles are M_2; green diamonds are M_3; purple squares are M_4; gold triangles are M_5. Plain black line is the exact steady-state solution. The reader is referred to the online version for color interpretation.*

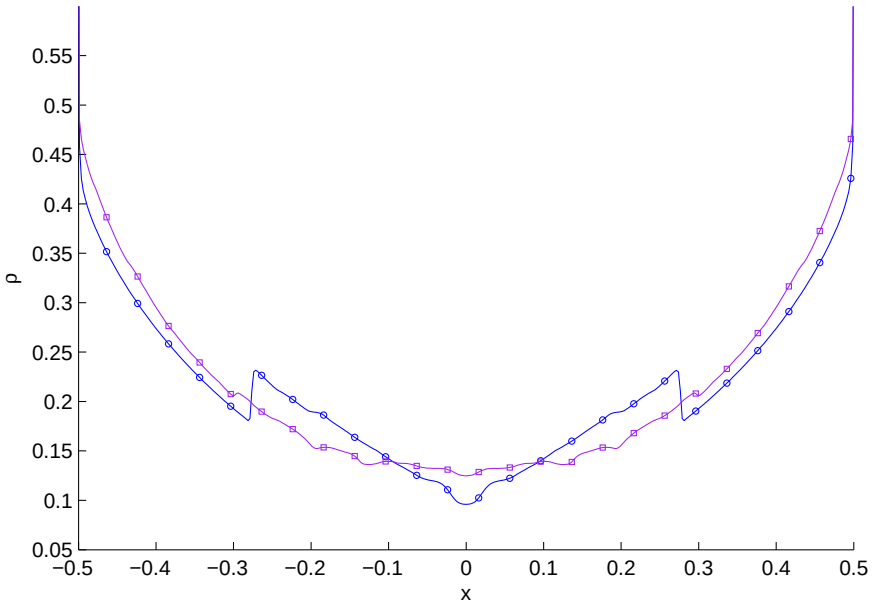

FIG. 4.2. *Transient solutions at $t = 1.0$. Blue circles are M_2; purple squares are M_4. The reader is referred to the online version for color interpretation.*

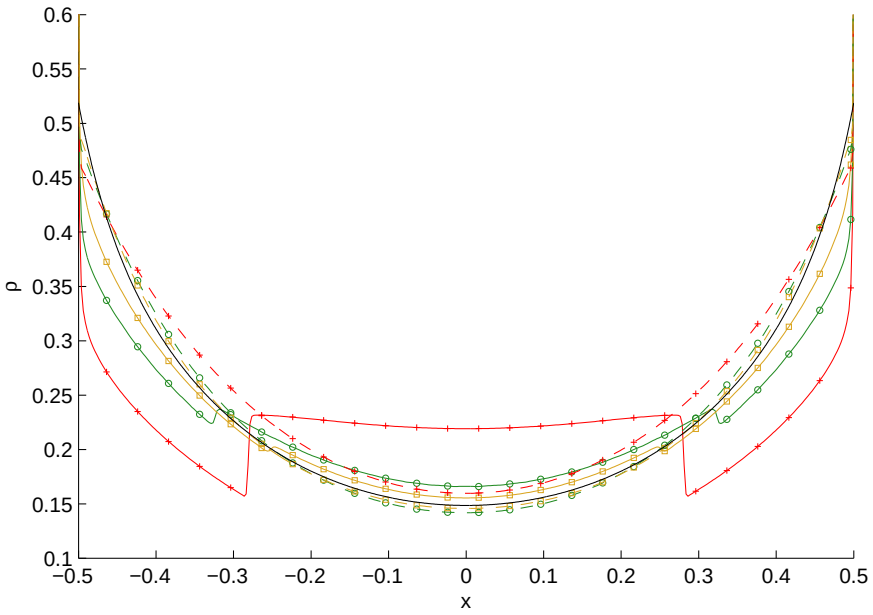

FIG. 4.3. *M_N (solid line) vs P_N (dashed line) for odd N. Red pluses are for M_1 and P_1; green diamonds are M_3 and P_3; Gold triangles are for M_5 and P_5. Plain black line is the exact steady-state solution. Reader is referred to the online version for color interpretation.*

to show a dip in the very center.[4] The odd solutions, on the other hand, appear to converge from below near the boundary and from above near the center. They also show a noticeable shock, in which the concentration jumps up when moving from the boundary toward the interior: at $x = \pm 0.28$ for M_1, $x = \pm 0.32$ for M_3 and $x = \pm 0.26$ for M_5. The size of this shock decreases as N increases. Previously it has been speculated that the reason for the M_1 shock was that the entropy reconstruction did not possess enough degrees of freedom to reproduce two opposing beams. However, these results point to something deeper, since the M_3 and M_5 solutions also display shocks.

We note that the even-N models also give rise to transient shocks. To show this, we display the M_2 and M_4 profiles at time $t = 1.0$ in Figure 4.2. Like the odd cases, these two shocks appear after the beams reach the center of the domain. However, they then disappear as they approach the boundary. The M_2 shock appears in the figure at $x = \pm 2.7$. The smaller M_4 shock appears at $x = \pm 3.0$. One can also see the formation of the center dip, particularly in the M_2 case. In addition both profiles include other transient oscillations which decay as the solution approaches steady state.[5]

In Figures 4.3 and 4.4, we compare the M_N solutions with standard P_N solutions, which are computed in *exactly* the same way, except that we replace G_j in (3.5) by

[4] We are not entirely sure whether or not this dip is a numerical artifact caused by small errors that arise when solving the dual optimization problem (2.11).

[5] We are also not completely sure whether these oscillations are numerical artifacts or not.

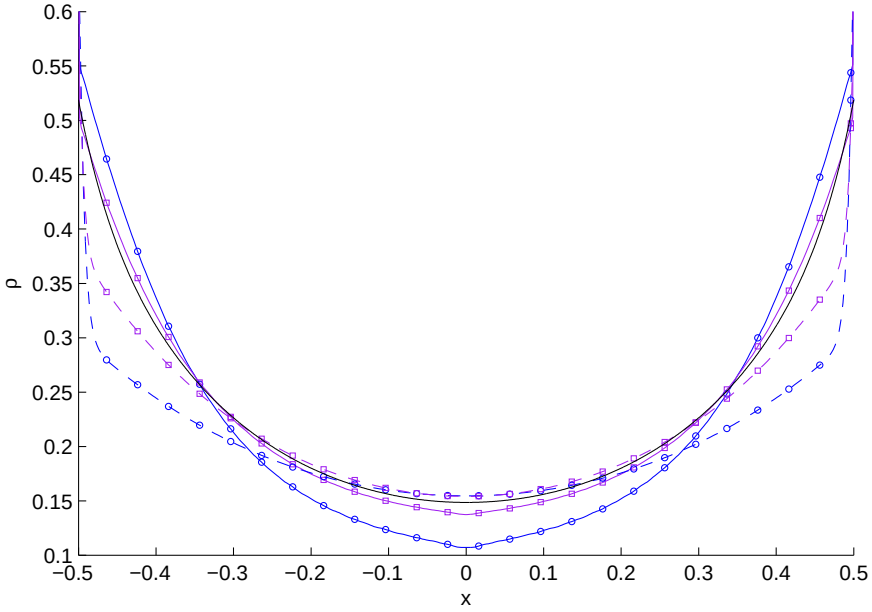

FIG. 4.4. *M_N (solid line) vs P_N (dashed line) for even N. Blue circles are for M_2 and P_2; purple squares are for M_4 and P_4. Plain black line is the exact steady-state solution. Reader is referred to the online version for color interpretation.*

$\mathbf{c}_j^T\mathbf{m}$, where

$$\mathbf{c}_j = \left\langle \mathbf{m}\mathbf{m}^T \right\rangle^{-1} \mathbf{u}_j \,. \tag{4.7}$$

The P_N equations are linear and thus do not produce shocks. However, it is well-known in the transport community (see, for example, [7]) that the P_N equations for even N are not accurate at boundaries. This fact is readily observed in Figure 4.4, where the M_N solutions are clearly better. For the odd case, the P_N solutions are more accurate; however, this is not always the case. For the test case in [5], for example, it is noted that the M_1 solution is qualitatively wrong (because of the shock), but quantitatively better than the corresponding P_1 solution.

4.2. Plane Source In the plane-source problem, particles are emitted from an initial plane source into an infinitely long medium. The symmetry of this problem allows it to be represented in the one-dimensional setting, where x measures the signed, normal distance to the plane. The plane-source problem is a torture test of a methods ability to handle very strong discontinuities. In the absence of any scattering, the P_N method represents the transport solution as a series of delta functions emanating from the initial source. Any scattering in the problem serves to smooth out these delta functions [4].

The plane source has been simulated with the M_1 closure in [5]. There it was found that the non-physical wave effects (from the delta functions) in P_N closures were less pronounced in the M_1 system. Moreover the M_1 system could move particles away from the source at peak speed (here equal to one), while particle speeds in linear P_N systems are limited by the maximum eigenvalue of the flux matrix. For low-

order closures, this value is significantly smaller than the maximum particle velocity: $1/\sqrt{3} \simeq 0.577$ for P_1 and approximately 0.861 for P_3. As N increases, the maximum eigenvalue eventually approaches one. Generally speaking, the P_N approximation is better for (i) longer times, (ii) larger scattering rates, and (iii) larger values of N.

We implement the plane-source problem assuming a purely scattering material with $\sigma_{\mathrm{t}} = \sigma_{\mathrm{a}} = 1.0$, with no source ($S = 0$) and initial condition

$$F_0(x, \mu) = 0.5\delta(x) + F_{\mathrm{floor}} \,, \tag{4.8}$$

where $F_{\mathrm{floor}} = 5.0 \times 10^{-5}$. Again a small, positive baseline value is used to maintain stability of the scheme, which is otherwise compromised by small errors in the solution of the optimization problem (2.11). Numerically, the delta function is represented with cell average values $0.25/\Delta x$ in the two center cells with a common edge at $x = 0$.

Although the problem is defined on an infinite domain, boundary conditions must be implemented in practice. To do so, we define a computational domain $[-L/2, L/2]$, where $L = 2t_{\mathrm{final}}+0.2$. This choice of L is large enough to ensure that the domain contains non-negligible features of the solution. At the endpoints, we apply the boundary condition

$$F_1(x, t) = F_2(x, t) = F_{\mathrm{floor}} \,. \tag{4.9}$$

We choose the spatial mesh size Δx based on the criteria that $\Delta x^2/L$ be roughly constant. For $t_{\mathrm{final}} = 1.0, 2.0, 4.0,$ and 6.0, this leads to $\Delta x = 0.005, 0.007, 0.01,$ and 0.0135, respectively.

Results for the plane source are given in Figures 4.5-4.8 at several different times and for several choices of N. A semi-analytic solution [14] is also provided as a benchmark. We make a conclusion similar to the one in [5]—namely, that the wave effects in the M_N profiles are less pronounced that in the P_N profiles. For the most part, the M_N profiles are qualitatively and quantitatively better than the P_N profiles.

5. Conclusions and Discussion

In this paper, we have presented computations of entropy-based (M_N) models for a linear transport equation with slab geometry. These computations were performed using a kinetic scheme that is formally second-order in space and can be first or second order in time.

The key difficulty in our computations is in solving the dual optimization problem for the coefficients $\boldsymbol{\alpha}$. Our algorithm, which uses the built in MATLAB function `fminunc`, does fairly well in most cases, but has trouble in regimes where the underlying kinetic distribution is beam-like. Even so, we are able to generate interesting results for two important test problems.

We conclude from our results that M_N models of all order may produce unphysical shocks, although the magnitude of such shocks becomes smaller as the size of the system increases. We observe also that, for even values of N, the M_N models behave better near the boundaries of the domain in the two-beam problem. However, it is still questionable in this case, whether M_N models produce better results than P_N models, which are cheaper to simulate on serial or moderately parallel architectures. For the plane-source problem, it appears that the M_N models yield better results than P_N.

Future work in this area is focused mainly on the solving the dual problem. It should be noted that some numerical work already exists; see, for example, [1,19] and references therein. While MATLAB provides an excellent interface for learning, the

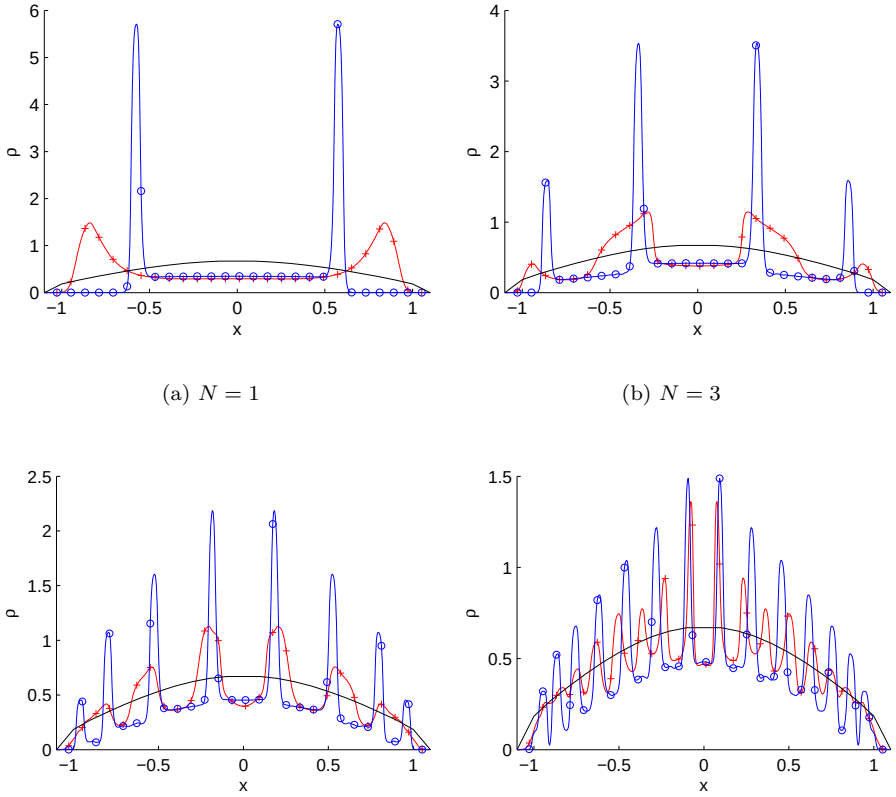

(a) $N = 1$ (b) $N = 3$

(c) $N = 7$ (d) $N = 15$

FIG. 4.5. *Planesource solution at $t = 1.0$. Red crosses are M_N. Blue circles are P_N. Solid black is the semi-analytic solution. The reader is referred to online version for color interpretation.*

computational effort required for the dual problem limits experimentation. Thus it will be necessary in the future to implement the scheme with a compiled language. Future efforts also include parallel implementation, which, as discussed in the Introduction, is one of the motivating factors for studying entropy-based methods.

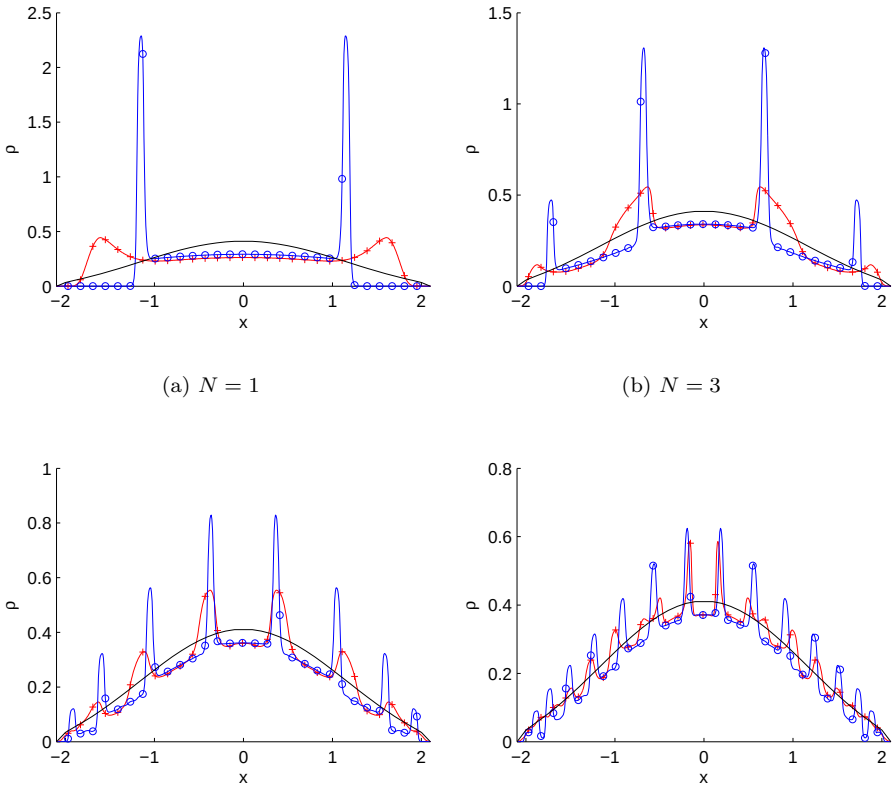

(a) $N = 1$

(b) $N = 3$

(c) $N = 7$

(d) $N = 15$

FIG. 4.6. *Planesource solution at $t = 2.0$. Red crosses are M_N. Blue circles are P_N. Solid black is the semi-analytic solution. The reader is referred to online version for color interpretation.*

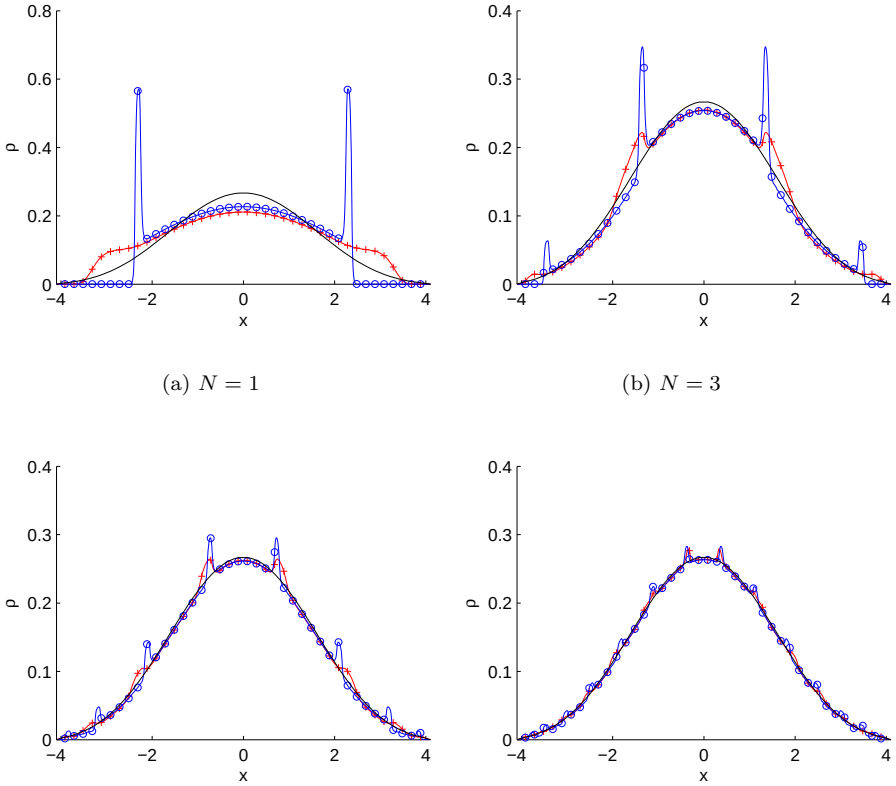

(a) $N = 1$ (b) $N = 3$

(c) $N = 7$ (d) $N = 15$

FIG. 4.7. *Planesource solution at $t = 4.0$. Red crosses are M_N. Blue circles are P_N. Solid black is the semi-analytic solution. The reader is referred to online version for color interpretation.*

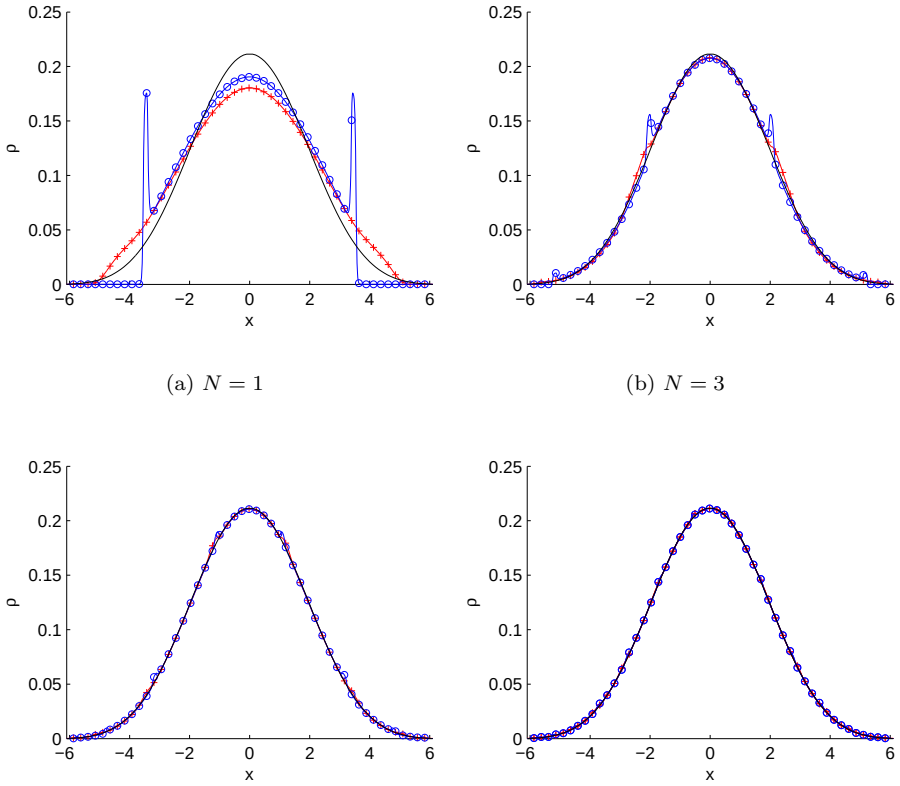

(a) $N = 1$ (b) $N = 3$

(c) $N = 7$ (d) $N = 15$

FIG. 4.8. *Planesource solution at $t = 10.0$. Red crosses are M_N. Blue circles are P_N. Solid black is the semi-analytic solution. The reader is referred to online version for color interpretation.*

6. Appendix: Proof of Theorem 4.1

The sole purpose of this appendix is to prove 4.1. We first show that the moments $\{u_1, \dots, u_N, u_{N+1}(\mathbf{u})\}$ are continuous at steady-state. Let $\mathbf{f}(\mathbf{u}) = [f_0(\mathbf{u}), \dots, f_N(\mathbf{u})]^T$ be the flux for the M_N system. Using the recursion relation for the Legendre polynomials [3], we can write

$$f_l(\mathbf{u}) \equiv \left\langle \mu m_l G_{\hat{\boldsymbol{\alpha}}(\mathbf{u})} \right\rangle = \begin{cases} u_1 \,, & l = 0 \\ \dfrac{l+1}{2l+1} u_{l+1} + \dfrac{l}{2l+1} u_{l-1} \,, & l > 0 \,. \end{cases} \tag{6.1}$$

For any $x \in [x_1, x_2]$ and any $\varepsilon > 0$ such that $x_1 < x - \varepsilon < x + \varepsilon < x_2$, weak solutions of the steady state M_N model satisfy

$$\mathbf{f}(\mathbf{u}(x+\varepsilon)) - \mathbf{f}(\mathbf{u}(x-\varepsilon)) = -\int_{x-\varepsilon}^{x+\varepsilon} \sigma_{\mathrm{t}} \mathbf{u} \, d\xi + \int_{x-\varepsilon}^{x+\varepsilon} \frac{\sigma_{\mathrm{s}}}{2} Q\mathbf{u} + \mathbf{s} \, d\xi \,. \tag{6.2}$$

If the quantities on the right are bounded, then letting $\varepsilon \to 0$ shows that the fluxes will be continuous. Using (6.1), one may then conclude that $u_1, ..., u_{N+1}$ are continuous at steady-state. However, nothing can be said about u_0.

We now show that if u_0 is discontinuous, then the mapping (4.2) cannot be injective. Define the quantities

$$\bar{\mathbf{u}} := \left[\frac{u_1}{u_0}, \dots, \frac{u_N}{u_0} \right]^T \,, \qquad \bar{\boldsymbol{\alpha}} := [\hat{\alpha}_1, \dots, \hat{\alpha}_N]^T \,, \tag{6.3}$$

$$\bar{\mathbf{m}} := [\mathbf{m}_1, \dots, \mathbf{m}_N]^T \,, \qquad G_{\bar{\boldsymbol{\alpha}}} := \exp(\bar{\boldsymbol{\alpha}}^T \bar{\mathbf{m}}) \,. \tag{6.4}$$

Then it is straight-forward to see that

$$\bar{\mathbf{u}} = \frac{\langle \bar{\mathbf{m}} G_{\bar{\boldsymbol{\alpha}}} \rangle}{\langle G_{\bar{\boldsymbol{\alpha}}} \rangle} =: \Phi(\bar{\boldsymbol{\alpha}}) \,. \tag{6.5}$$

The Jacobian of Φ is positive definite, since for any nonzero vector $\mathbf{v} \in \mathbb{R}^{N-1}$,

$$\mathbf{v}^T \frac{\partial \Phi}{\partial \bar{\mathbf{u}}} \mathbf{v} = \frac{\langle G_{\bar{\boldsymbol{\alpha}}} \rangle \langle (\mathbf{v}^T \bar{\mathbf{m}})^2 G_{\bar{\boldsymbol{\alpha}}} \rangle - \langle \mathbf{v}^T \bar{\mathbf{m}} G_{\bar{\boldsymbol{\alpha}}} \rangle^2}{\langle G_{\bar{\boldsymbol{\alpha}}} \rangle^2} > 0. \tag{6.6}$$

This inequality follows by applying the Cauchy-Schwarz inequality to the second term of the numerator with $g_1 := G_{\bar{\boldsymbol{\alpha}}}^{1/2} (\mathbf{v}^T \bar{\mathbf{m}})$ and $g_2 := G_{\bar{\boldsymbol{\alpha}}}^{1/2}$. The fact that g_1 and g_2 cannot be co-linear implies that the numerator is positive. Meanwhile, the denominator is obviously positive.

The fact that Jacobian is positive definite means that Φ can be inverted globally to determine $\bar{\boldsymbol{\alpha}}$ as a smooth function of $\bar{\mathbf{u}}$. Hence the normalized moment

$$\chi(\bar{\mathbf{u}}) := \frac{u_{N+1}}{u_0} \equiv \frac{\langle m_{N+1} G_{\bar{\boldsymbol{\alpha}}} \rangle}{\langle G_{\bar{\boldsymbol{\alpha}}} \rangle} \,, \tag{6.7}$$

which depends only on $\bar{\boldsymbol{\alpha}}$, can be expressed as a function of $\bar{\mathbf{u}}$ only, rather than $\mathbf{u}$. We denote this function by χ; it is a generalized Eddington factor. Now for $1 \le k \le N$, the ratios

$$\frac{u_{N+1}}{u_k} \equiv \frac{\chi(\bar{\mathbf{u}})}{\bar{u}_k} \tag{6.8}$$

are all continuous because, as already proven, the moments $\{u_1, \ldots, u_{N+1}\}$ are all continuous. In addition, these ratios depend only on $\bar{\mathbf{u}}$. Hence if the mapping (4.2) is injective, $\bar{\mathbf{u}}$ must also be continuous and, hence, u_0 as well. This proves the result by contraposition.

REFERENCES

[1] R. Abramov, *The multidimensional maximum entropy moment problem: A review on numerical methods*, Communications in Mathematical Sciences, 8 (2009), pp. 377–392.

[2] A. Anile, W. Allegretto, and C. Ringhofer, *Mathematical Problems in Semiconductor Physics*, vol. 1823 of Lecture Notes in Mathematics, Springer-Verlag, Berlin, 2003. Lectures given at the C.I.M.E. Summer School held in Cetraro, Italy on July 15-22, 1998.

[3] G. B. Arfken and H. J. Weber, *Mathematical Methods for Physicists*, Academic Press, San Diego, 4th ed., 1995.

[4] T. A. Brunner, *Riemann Solvers for Time-Dependent Transport Based on the Maximum Entropy and Spherical Harmonics Closures*, PhD thesis, University of Michigan, 2000.

[5] T. A. Brunner and J. P. Holloway, *One-dimensional Riemann solvers and the maximum entropy closure*, J. Quant Spect. and Radiative Trans, 69 (2001), pp. 543 – 566.

[6] R. Dautray and J. L. Lions, *Mathematical Analysis And Numerical Methods For Science And Technology, Volume 6: Evolution Problems II*, Spinger-Verlag, Berlin, 2000.

[7] B. Davison, *Neutron Transport Theory*, Oxford University Press, London, 1973.

[8] S. M. Deshpande, *Kinetic theory based new upwind methods for inviscid compressible flows*, in American Institute of Aeronautics and Astronautics, New York, 1986. Paper 86-0275.

[9] W. Dreyer, M. Herrmann, and M. Kunik, *Kinetic solutions of the Boltzmann-Peierls equation and its moment systems*, Continuum Mechanics and Thermodynamics, 16 (2004), pp. 453–469.

[10] B. Dubroca and J.-L. Fuegas, *Étude théorique et numérique d'une hiérarchie de modèles aus moments pour le transfert radiatif*, C.R. Acad. Sci. Paris, I. 329 (1999), pp. 915–920.

[11] B. Dubroca and A. Klar, *Half-moment closure for radiative transfer equations*, J. Comput. Phys., 180 (2002), pp. 584–596.

[12] M. Frank. Private communication, 2010.

[13] M. Frank, B. Dubroca, and A. Klar, *Partial moment entropy approximation to radiative heat transfer*, J. Comput. Phys., 218 (2006), pp. 1–18.

[14] B. D. Ganapol, *Homogeneous infinite media time-dependent analytic benchmarks for X-TM transport methods development*, tech. rep., Los Alamos National Laboratory, March 1999.

[15] S. Gottlieb and C.-W. Shu, *Total variation diminishing Runge-Kutta schemes*, Math. Comput., 67 (1998), pp. 73–85.

[16] C. Groth and J. McDonald, *Towards physically realizable and hyperbolic moment closures for kinetic theory*, Continuum Mechanics and Thermodynamics, (2009).

[17] A. Harten, P. D. Lax, and V. Leer, *On upstream diferencing and Godunov-type schemes for hyperbolic conservation laws*, SIAM Rev., 25 (1983), pp. 35–61.

[18] C. D. Hauck, C. D. Levermore, and A. L. Tits, *Convex duality and entropy-based moment closures: Characterizing degenerate densities*, SIAM J. Control Optim., 47 (2008), pp. 1977–2015.

[19] W. Huang, *Heuristic solutions to polynomial moment problems with some convex entropic objectives*, Numerical Algorithms, 12 (1996), pp. 297–308.

[20] S. Jin and C. D. Levermore, *Numerical schemes for hyperbolic systems of conservation laws with stiff diffusive relaxation*, J. Comput. Phys., 126 (1996), pp. 449–467.

[21] M. Junk, *Domain of definition of Levermore's five moment system*, J. Stat. Phys., 93 (1998), pp. 1143–1167.

[22] ———, *Maximum entropy for reduced moment problems*, Math. Mod. Meth. Appl. S., 10 (2000), pp. 1001–1025.

[23] M. Junk and V. Romano, *Maximum entropy moment system of the semiconductor Boltzmann equation using Kane's dispersion relation*, Continuum Mechanics and Thermodynamics, 17 (2005), pp. 247–267.

[24] E. W. Larsen and C. G. Pomraning, *The P_N theory as an asymptotic limit of transport theory in planar geometry—I: Analysis*, Nucl. Sci. Eng, 109 (1991), pp. 49–75.

[25] ———, *The P_N theory as an asymptotic limit of transport theory in planar geometry—II: Numerical results*, Nucl. Sci. Eng., 109 (1991), pp. 76–85.

[26] C. D. Levermore, *Boundary conditions for moment closures.* Presented at Institute for Pure

and Applied Mathematics University of California, Los Angeles, CA on May 27, 2009.
[27] ———, *Moment closure hierarchies for kinetic theory*, J. Stat. Phys., 83 (1996), pp. 1021–1065.
[28] E. E. Lewis and J. W. F. Miller, *Computational Methods in Neutron Transport*, John Wiley and Sons, New York, 1984.
[29] R. B. Lowrie and J. E. Morel, *Methods for hyperbolic systems with stiff relaxation*, Int. J. Numer. Meth. Fluids, 40 (2002), pp. 413–423.
[30] P. A. Markowich, C. A. Ringhofer, and C. Schmeiser, *Semiconductor Equations*, Springer-Verlag, New York, 1990.
[31] S. A. McKee, W. A. Wulf, and T. C. Landon, *Bounds on memory bandwidth in streamed computations*, in Euro-Par '95: Proceedings of the First International Euro-Par Conference on Parallel Processing, London, UK, 1995, Springer-Verlag, pp. 83–99.
[32] G. N. Minerbo, *Maximum entropy Eddington factors*, J. Quant. Spectrosc. Radiat. Transfer, 20 (1978), pp. 541–545.
[33] P. Monreal and M. Frank, *Higher order minimum entropy approximations in radiative transfer*. preprint.
[34] B. Perthame, *Boltzmann type schemes for gas dynamics and the entropy property*, SIAM J. on Numer. Anal., 27 (1990), pp. 1405–1421.
[35] B. Perthame, *Second-order Boltzmann schemes for compressible euler equations in one and two space dimensions*, SIAM J. Numer. Anal., 29 (1992), pp. 1–19.
[36] G. C. Pomraning, *Variational boundary conditions for the spherical harmonics approximation to the neutron transport equation*, Ann. Phys., 27 (1964), pp. 193–215.
[37] G. C. Pomraning, *Radiation Hydrodynamics*, Pergamon Press, New York, 1973.
[38] S. L. Rosa, G. Mascali, and V. Romano, *Exact maximum entropy closure of the hydrodynamical model for Si semiconductors: The 8-moment case*, SIAM Journal on Applied Mathematics, 70 (2009), pp. 710–734.
[39] J. Schneider, *Entropic approximation in kinetic theory*, Math. Model. Numer. Anal., 38 (2004), pp. 541–561.
[40] C.-W. Shu and S. Osher, *Effcient implementation of essentially non-oscillatory shock capturing schemes*, J. Comp. Phys., 77 (1988), pp. 439–471.
[41] H. Struchtrup, *Kinetic schemes and boundary conditions for moment equations*, Z. Angew. Math. Phys., 51 (2000), pp. 346–365.
[42] D. Wright, M. Frank, and A. Klar, *The minimum entropy approximation to the radiative transfer equation*. preprint.
[43] W. A. Wulf and S. A. McKee, *Hitting the memory wall: implications of the obvious*, SIGARCH Comput. Archit. News, 23 (1995), pp. 20–24.